

УДК 539.172.8

ISOTOPIC TRENDS IN NUCLEAR MULTIFRAGMENTATION

*M. Veselsky**

Institute of Physics, Slovak Academy of Sciences, Bratislava

INTRODUCTION	400
MULTIFRAGMENTATION THEORY AND RELATED TOPICS	402
EXPERIMENTAL ASPECTS OF MULTIFRAGMENTATION STUDIES	408
ISOTOPIC TRENDS	416
THERMODYNAMICAL PROPERTIES OF THE HOT QUASI- PROJECTILES	426
SUMMARY AND CONCLUSIONS	432
REFERENCES	433

*E-mail: fyzimarv@savba.sk

УДК 539.172.8

ISOTOPIC TRENDS IN NUCLEAR MULTIFRAGMENTATION

*M. Veselsky**

Institute of Physics, Slovak Academy of Sciences, Bratislava

An overview of the recent progress in the studies of nuclear multifragmentation is presented. Special emphasis is put on the exploration of isotopic trends in nuclear multifragmentation and the possibilities of extracting physical information related to the nuclear equation of state. Relevant experimental methods of isotope identification are described. The isotopic composition of fragments is used to extract the values of thermodynamical observables of the system undergoing multifragmentation such as temperature and chemical potentials. Various methods for extraction of thermodynamical variables are analyzed. An overview of methods of isotope thermometry, exploring the sensitivity of various yield ratios to temperature, is presented. An exponential scaling of relative isotopic yields from reactions with different neutron content, called isoscaling, is used to explore the evolution of the isospin degrees of freedom of the system. Finally, the nuclear equation of state and the isospin-asymmetric liquid–gas phase transition in the nuclear matter are discussed.

Представлен обзор последних достижений в изучении мультифрагментации ядер. Особое внимание уделяется исследованию изотопических зависимостей при ядерной мультифрагментации и возможности извлечения физической информации, относящейся к уравнению состояния ядра. Описываются подходящие экспериментальные методы идентификации изотопов. Изотопический состав фрагментов используется для определения величин термодинамических наблюдаемых системы, подвергаемой мультифрагментации, а именно температуры и химических потенциалов. Проводится анализ различных методов извлечения термодинамических переменных. Представлен обзор методов термометрии изотопов, исследующих чувствительность различных отношений выходов к температуре. Экспоненциальный скейлинг относительного изотопического состава из реакций с различным содержанием нейтронов, называемый изоскейлингом, используется для исследования поведения изоспиновых степеней свободы системы. Наконец, обсуждаются уравнение состояния ядра и изоспиново-асимметричный фазовый переход жидкость–газ ядерной материи.

INTRODUCTION

Experimental studies, carried out during last two decades (for review see [1] and for update of the recent progress see, e.g., [2]), demonstrate that, in nuclear reactions such as the nucleus–nucleus collisions in the Fermi energy domain or the collisions of a high-energy light particle with a heavy target, the amount of kinetic energy dissipated into the internal excitation energy is large enough to produce

*E-mail: fyzimarv@savba.sk

highly excited (hot) nuclei which may further deexcite via multifragmentation, a decay mode where the hot nucleus disintegrates into many fragments. In the nature, nuclear processes of such a type can be observed in the interaction of cosmic rays with terrestrial and interplanetary matter. Such spallation reactions contribute to the observed isotopic composition of the interstellar matter which can be used to study the properties of the cosmic rays and of their astrophysical sources (for review see, e.g., [3]). With the advent of powerful accelerators of high-energy particles and, more recently, of heavy ions of intermediate and high energy, it became possible to study the process of multifragmentation in the laboratory. Extensive experimental studies of multifragmentation are conducted since eighties of the last century. As can be deduced from observed experimental data [1,2], during the process of multifragmentation the nuclear medium becomes hot, expands and is supposed to undergo a phase transition where two phases are created — a dense isospin-symmetric phase (liquid) and a dilute isospin-asymmetric phase (vapor or gas). Such a phase transition was predicted by theory (for review see [4]). The most common theoretical description of multifragmentation is based on the statistical model of multifragmentation [5], typically assuming a thermally equilibrated freeze-out configuration with hot (excited) or cold fragments. The probabilities of various fragment partitions can be evaluated analytically using the grand-canonical approach. While the statistical model of multifragmentation is quite successful in describing a wide range of fragment observables, it does not provide a specific information on the mechanism of the underlying process of fragment formation, apart from the assumption that at the freeze-out configuration a thermal equilibrium among the fragments is reached. The underlying process of cluster formation can be related to the equation of state of asymmetric nuclear matter at subsaturation densities, where the phase transition is supposed to occur. The coexistence line, typical for the one-component system such as symmetric nuclear matter, develops with introduction of isospin asymmetry into a complex coexistence region [6], typically suggesting a coexistence of the dilute isospin-asymmetric phase and isospin-symmetric dense phase. Further theoretical investigations [7] suggest that instability modes responsible for the phase transition are typically combinations of mechanical and chemical instability modes.

In this article, we present an overview of the recent progress in the studies of nuclear multifragmentation. We place a special emphasis on the exploration of isotopic trends in nuclear multifragmentation and the possibilities to extract physical information related to the nuclear equation of state. Experimental studies of isotopic trends in nuclear multifragmentation have been made possible by using the state-of-the-art detection techniques, which allow one to identify individual isotopes of light charged particles and intermediate mass fragments in wide angular ranges. The isotopic composition of fragments can be used to extract the values of thermodynamical observables of the system undergoing multifragmentation such as temperature and chemical potentials (free nucleon densities). Various

methods for extraction of temperature from isotopic composition are analyzed. An exponential scaling of the yields of specific isotopes from different reactions with the isotope neutron and proton numbers (isoscaling) is used to study the evolution of the isospin degrees of freedom of the system. Finally, the nuclear equation of state and the isospin-asymmetric liquid–gas phase transition in the nuclear matter are discussed.

MULTIFRAGMENTATION THEORY AND RELATED TOPICS

Multifragmentation is a process where the final state consists of multiple fragments which are the remnants of a hot nucleus (Fig. 1). The aim of the multifragmentation theory is to relate the properties of final fragments to properties of the original hot nucleus. Statistical phase-space models of multifragmentation

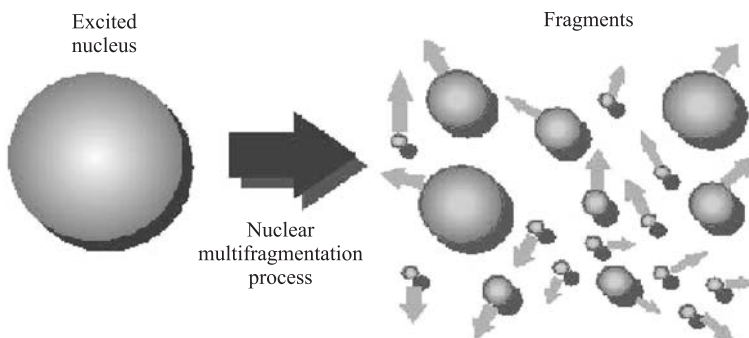


Fig. 1. A schematic view of multifragmentation

typically assume that the properties of final fragments are determined in the so-called «freeze-out» configuration, where the typical distance of prefragments becomes, due to thermal expansion, larger than the radius of the short-range nuclear interaction. It is, however, difficult to study the properties of the freeze-out configuration using the experimentally observed final fragments without additional model assumptions reflecting the reaction mechanism by which the hot nucleus was created. A detailed knowledge of the reaction mechanisms contributing to production of hot nuclei is necessary to properly characterize initial conditions of multifragmentation. The production of hot nuclei can be treated separately as a stage prior to multifragmentation, assuming that statistical equilibrium will be reached at later stage (typically at freeze-out). In a microscopic description of nuclear medium, multifragmentation can be related to a phase transition into dense and dilute phase. Isospin asymmetry of two phases may be different. Furthermore, multifragmentation can be treated dynamically using the transport theory. Such treatment offers the possibility to study the evolution of the nuclear medium

during the whole process, including the conditions for the isospin-asymmetric phase transition. In this section we briefly review the most relevant aspects of the multifragmentation theory and related reaction theory.

Statistical Phase-Space Models of Multifragmentation. A main assumption of the statistical phase-space models describing various processes is that a certain stage of the process can be identified where the available phase-space determines the final probability distribution of exit channels. For instance, in statistical description of the fully equilibrated compound nucleus, the probabilities of various evaporation channels are determined by available phase space of the corresponding evaporation residue and the fission probability is determined by available phase space at the saddle-point on top of the fission barrier. In the case of simultaneous multifragmentation, the phase-space is explored for the possible multifragment configurations (partitions), typically at the stage where short-range nuclear interaction freezes out and the identities of final fragments are determined. This is the so-called «freeze-out» configuration. The probabilities of various partitions can be determined statistically, exactly using the microcanonical ensemble [8], or approximately using the canonical and grand-canonical ensembles [5]. Canonical and grand-canonical approximations typically reduce the mathematical complexity while raising questions on the applicability of such approximations since the nuclei are rather small systems. Detailed discussion of the application of statistical mechanics to small systems can be found in [9].

Here we briefly review the most commonly used phase-space model of multifragmentation, the Statistical Model of Multifragmentation (SMM) [5]. The model uses the grand-canonical approximation, the freeze-out volume depends on fragment multiplicity, and internal excitation of fragments in the freeze-out configuration is considered, thus producing «hot» fragments. Analogous models with «cold» fragments also exist [8], typically the freeze-out volume is chosen approximately twice larger than in the case of hot fragments. Yield of fragments with neutron and proton numbers N and Z can be, within grand-canonical approach, characterized by formula [5]:

$$Y(N, Z) = g_{NZ} \frac{V_f}{\lambda_T} A^{3/2} \exp(-(1/T)(F_{NZ}(T, V) - N\mu_n - Z\mu_p)), \quad (1)$$

where g_{NZ} is the ground state spin degeneracy; V_f is the free volume ($V_f = V - V_0$, where V and V_0 are the volumes at freeze-out and ground state); λ_T is the thermal wavelength; F_{NZ} is the intrinsic free energy of the fragment; μ_n and μ_p are the free neutron and proton chemical potentials, and T is the temperature. The free volume at freeze-out is determined as $V_f = \chi V_0$. The parameter χ is determined as

$$\chi = \left(1 + \frac{d}{r_0 A_0^{1/3}} (M^{1/3} - 1) \right)^3 - 1, \quad (2)$$

where M is the fragment multiplicity; d is nuclear diffuseness; A_0 is the mass of the system; and r_0 is the nuclear radius parameter. It is essentially a product of the additional fragment surface area and nuclear diffuseness length. The values of χ range from 0.2 to 2. The fragment free energy is at most part determined using the liquid drop model. The component of the free energy corresponding to the Coulomb interaction is determined using the Wigner–Seitz approximation. The Wigner–Seitz clusterization energy is calculated at volume $V = (1 + \kappa)V_0$. The value of κ can be related to average Coulomb barrier and thus is generally different from χ , which controls the freeze-out of strong interaction. Typical value is $\kappa = 3.5$ which is between the values for closely packed fragments ($\kappa = 2$) and for fission ($\kappa = 5$). The statistical model of multifragmentation was used for extensive comparisons with experimental multifragmentation data, typically obtaining a consistent description of a wide range of experimental observables [5, 10, 11].

As an alternative to models of simultaneous multifragmentation, the traditional model of compound nucleus decay based on Hauser–Feshbach approximation [12] was extended to describe the emission of intermediate mass fragments (IMF) [13]. The emission of such complex fragments is described as a binary split, essentially an asymmetric fission where the IMF is accompanied by a heavy residue. The emission probability is determined by a value of the mass-asymmetric fission barrier height. The model of fission-like binary split describes reasonably well the onset of fragment emission, thus indicating that at the onset the complex fragment emission is a fission-like process [14]. Success of such approach prompted the attempts to describe multifragmentation using the model of Sequential Binary Decay (SBD). Several implementations (e.g., the GEMINI code [15]) have been used extensively for comparisons with experimental multifragmentation data, with reasonable success in description of, e.g., inclusive mass and charge distributions. However, the model of sequential binary decay fails to describe the results of the exclusive measurements at the zero angle [11] allowing one to select a narrow region around the multifragmentation threshold while SMM performs rather well. An explanation is suggested by comparison of the model of sequential binary decay to transitional-state model of multifragmentation [16] where even for binary exit channel the number of available degrees of freedom is different. Furthermore, the model of sequential binary decay also fails to reproduce the observed fragment correlations [17].

Isospin-Asymmetric Liquid–Gas Phase Transition. Phase-space models of multifragmentation typically explore the properties of final fragments in the freeze-out configuration where nuclear interaction between the fragments does not play a role. The underlying mechanism leading to multifragmentation is nevertheless closely related to properties of the nuclear medium, which can be studied microscopically. Over the recent decades, thermal properties of the nuclear medium were studied theoretically using microscopic approaches such as temperature-dependent Hartree–Fock [18] or relativistic mean-field [6] approxi-

mations. The microscopic theory of the nuclear matter predicts a phase transition of the liquid–gas type (Fig. 2). Below a critical temperature, two phases can coexist. The spatial distribution of phases can be expected to develop from vapor bubbles in liquid at a high density toward liquid droplets in vapor at low densities [19]. A hot nucleus undergoing multifragmentation can be envisioned as rapidly expanding until it enters the spinodal region. At that stage multifragmentation occurs due to rapidly developing dynamical instabilities. When considering the isospin-asymmetric nuclear matter [6, 20], the phase transition is supposed to lead to separation into a symmetric dense phase and asymmetric dilute phase. It has been discussed in literature [7] to what extent such a phase transition is generated by fluctuations of density or concentration, typically suggesting a coupling of different instability modes.

The properties of clusters formed in the phase transition can be described by a variety of random cluster models. Simple model of clusterization was proposed by Fisher [21], where the liquid drop expansion of the Gibbs free energy leads to the mass distribution of clusters

$$P(A) \propto A^{-\tau} \exp(-b(T)A^{2/3}), \quad (3)$$

where the surface term $b(T) = 4\pi r_0^2 \sigma(T)/T$ decreases monotonically toward zero as temperature approaches critical temperature T_c . At critical temperature the mass distribution becomes a power law with the critical exponent τ . Similar properties are obtained using percolation models, lattice models, and cellular model of fragmentation (an extensive overview of these models in the context of multifragmentation can be found in [4], sections 4, 5).

Calculations based on the microscopic nuclear theory [6, 20] suggest that nuclear matter undergoes liquid–gas phase transition which is of the first order, the density difference between phases being the order parameter. Similar conclusions can be obtained also in the context of SMM [22]. However, the phase transition in the percolation models is of the second order and lattice models such as Ising model [23] exhibit a complex phase diagram with both the first and the second order phase transitions. Furthermore, since theory of nuclear phase transitions is formulated for infinite systems, while the experiments investigate multifrag-

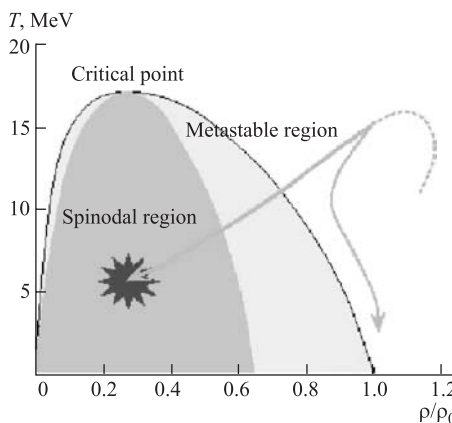


Fig. 2. A schematic description of the nuclear liquid–gas phase transition as a mechanism of multifragmentation

mentation of finite nuclei, it is necessary to assess the effect of finite size. As discussed in [4], the critical behavior observed in random-cluster models can be related to scaling properties and self-similarity of the system at different scales, what suggests that observed properties of the finite system represent the properties of infinite media. On the other hand, finiteness constraints of small systems can lead to a behavior analogous to criticality [4]. Obviously, for any experimental observation the effect of finite size should be assessed.

Production of Hot Nuclei. The statistical multifragmentation theory typically does not explicitly consider the evolution of the system prior to the freeze-out (or underlying phase transition). Usually it is difficult to determine the properties of the freeze-out configuration using the experimentally observed final fragments without additional model assumptions reflecting the reaction mechanism by which the hot nucleus was created. A detailed knowledge of the reaction mechanisms

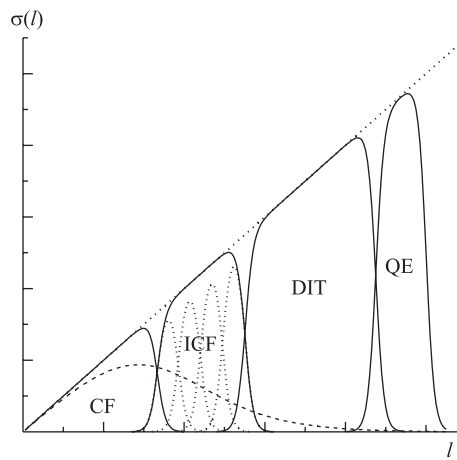


Fig. 3. Development of the reaction mechanisms in nucleus–nucleus collisions in the Fermi energy domain. Cross-section contributions are plotted schematically as a function of the initial angular momentum

nucleus–nucleus collisions in the Fermi energy domain (20–50 $A \cdot \text{MeV}$) depending on the impact parameter, projectile–target asymmetry, and the projectile energy (Fig. 3). The reaction mechanisms typically observed are [24]:

- peripheral elastic and quasi-elastic (QE) scattering/transfer reactions around the grazing impact parameter;
- deep inelastic transfer (DIT) reactions at semiperipheral impact parameters with partial overlap of the projectile and target and a significant part of the relative

contributing to production of hot nuclei is necessary to properly characterize initial conditions of multifragmentation and to verify the model assumptions used by multifragmentation theory.

In order to undergo multifragmentation, intrinsic excitation energy of the hot massive nuclei should exceed $2\text{--}3 A \cdot \text{MeV}$. Such excitation energies can be reached in nucleus–nucleus collisions with the nuclear beams of intermediate energies (20–100 $A \cdot \text{MeV}$). In collisions of a high-energy light particle with a heavy target the necessary energies range from hundreds of $A \cdot \text{MeV}$ to $A \cdot \text{GeV}$. These are the reaction domains which have been used extensively for multifragmentation studies.

A large variety of reaction mechanisms has been observed in nucleus–

kinetic energy transferred into internal excitation energies of the projectile and target;

— incomplete fusion (ICF) reactions at central impact parameters with a typical participant-spectator scenario. At energies around the Fermi energy the participant zone typically fuses with one of the spectator zones (typically heavier) thus creating a highly excited composite nucleus. At most central impact parameters the complete fusion (CF) can occur;

— pre-equilibrium emission of direct particles, caused by onset of two-body nucleon–nucleon collisions at central and midperipheral impact parameters. Pre-equilibrium emission typically precedes the ICF/CF and DIT reactions.

While such a scheme is rather well justified by experimental data [24], there are still many open questions related to the reaction mechanism, specifically concerning the development of isospin-asymmetry in nucleus–nucleus collisions in the Fermi energy domain. Studies of isospin degrees of freedom in the nucleus–nucleus collisions in the Fermi energy domain reveal many interesting details of the reaction scenario. Recently, an enhancement in the production of neutron-rich nuclei was observed in peripheral nucleus–nucleus collisions [25], which can be related to the effect of neutron-rich surface of the target.

At projectile energies of hundreds of $A \cdot \text{MeV}$ and above, the impinging light particle initiates an intranuclear cascade [26] of nucleon–nucleon collisions which is the main mechanism leading to the production of hot nuclei. The heavy remnant after the intranuclear cascade is highly excited and typically undergoes multifragmentation at a wide range of impact parameters [5]. In nucleus–nucleus collisions at similar energies the participant zone develops independently of two spectator zones and typically disintegrates due to intense cascade of nucleon–nucleon collisions, with the possibility to produce subnuclear particles via excitation of hadronic degrees of freedom. The spectator zones are relatively colder, nevertheless typically hot enough to undergo multifragmentation [27].

Dynamical Description of Multifragmentation. As an alternative to two-step reaction scenario, where reaction dynamics is attributed to, the early stage of nucleus–nucleus collision while multifragmentation of the hot nucleus is described statistically, the whole process can be described in unified fashion by dynamical theory with explicit time-dependence.

In the microscopic time-dependent Hartree–Fock theory [28] — an extension of the Hartree–Fock theory of the ground state — the nucleus–nucleus collision is represented by time evolution of the one-body mean field, which defines the collective degrees of freedom of the system. The time-dependent Hartree–Fock theory does exhibit collective behavior which reminds many experimentally observed phenomena [28], it nevertheless does not include two-body dissipation via collisions of nucleons which is supposed to play significant role at energy regimes where the hot nuclei are produced.

Two-body interaction can be included in the framework of quantum kinetic theory as represented by the Boltzmann transport equation, which describes the reaction dynamics in terms of both mean-field and two-body dissipation. Various semiclassical methods featuring the concept of pseudoparticle are used to simulate the solution of the Boltzmann transport equation. The most common approximations are Vlasov–Uhling–Uhlenbeck (VUU) [29], Boltzmann–Uhling–Uhlenbeck (BUU) [30], Landau–Vlasov (LV) [31], Boltzmann–Nordheim–Vlasov (BNV) [32] and Quantum Molecular Dynamics (QMD) [33] methods. Results of such simulations usually offer a qualitative description of the main features of reaction dynamics including multifragmentation. Using the transport theory, the properties of the nuclear equation of state such as nuclear incompressibility and symmetry energy can be investigated phenomenologically.

EXPERIMENTAL ASPECTS OF MULTIFRAGMENTATION STUDIES

Experimental studies of isotopic trends in nuclear multifragmentation were enabled by the recent progress in acceleration and detection techniques. A crucial condition is an unambiguous isotopic identification of detected fragments, which can be achieved using high-resolution particle telescopes. In order to reconstruct the multifragmenting system and to understand the production mechanism of the hot nuclei it is desirable to detect the charged particles in a wide angular range, ideally in the 4π geometry. In this section we briefly review the experimental devices (using the facilities installed at Texas A&M University as examples) and essential methods relevant to the studies of isospin degrees of freedom in nuclear multifragmentation.

Arrays of Charged Particle Detectors with Large Angular Coverage. During the process of multifragmentation, multiple charged particles are emitted in a wide angular range. Angular distribution of fragments in the laboratory frame is determined by the production mechanism of the hot nucleus and by the choice of the projectile and target nuclei. The design of arrays of charged particle detectors must be optimized in order to detect and resolve emitted charged particles from the expected multifragmentation source. This can be achieved by the choice of angular coverage, granularity, and detection thresholds.

A state-of-the-art forward array, the multidetector array FAUST [34], installed at the Cyclotron Institute of Texas A&M University, covers forward angles between $2\text{--}35^\circ$ where the fragments originating from the projectile-like source can be expected. It consists of 68 charged particle telescopes arranged into 5 rings. Each particle telescope consists of $300\ \mu\text{m}$ thick silicon detector followed by 3 cm thick CsI(Tl) crystal. Angular ranges covered by the rings are chosen in order to distribute the multiplicity of detected particles evenly, thus avoiding the cases when one telescope is hit by multiple particles. The mass and atomic number of

the detected charged particles can be identified up to $Z = 6$. Forward arrays such as FAUST are optimized for the study of projectile multifragmentation, specifically for asymmetric reactions where target nucleus is much heavier than the projectile.

In order to study symmetric reactions where a hot composite source is created it is necessary to cover the largest possible angular range, ideally 4π . For instance, the multidetector NIMROD [35] at the Cyclotron Institute of Texas A&M University provides such a coverage using 96 detector modules arranged in 12 rings. Light charged particles ($Z \leq 2$) are detected and identified in the whole range while a subset of modules (2 per ring) offer isotopic identification up to $Z = 8$. Furthermore, atomic number of heavy residues can be resolved using ionization chambers and neutron multiplicity can also be determined since the array is surrounded by a 4π neutron multiplicity counter (neutron ball).

Identification of Isotopes. An important step in the off-line analysis of data from the multidetector arrays with large angular coverage such as FAUST and NIMROD is to identify as many fragment species as possible. The method of isotope identification is based on the well-known particle telescope technique in which the isotopes are resolved in two-dimensional $\Delta E - E$ spectra of energy losses in two detectors (typically a thin one followed by a thick one). We developed and successfully used [36] a method which enables one to carry out identification and energy calibrations simultaneously using a minimization procedure applied to two-dimensional spectra.

In the experimental spectra, the lines for three known isotopes (typically the most characteristic isotopes such as ^1H , ^4He , ^9Be) are assigned, and calibration is carried out by a minimization procedure where these lines are fitted to corresponding calculated energy losses for a given $\Delta E - E$ telescope. The calibration coefficients are thus obtained as optimum values of minimization parameters.

An example of the calibrated two-dimensional spectrum of Si-Si telescope is shown in Fig. 4 along

with the calculated $\Delta E - E$ lines for a wide range of isotopes. The data used were collected in ring 8 of the NIMROD array in the reaction $^{124}\text{Sn} + ^{124}\text{Sn}$ at $28 A \cdot \text{MeV}$. For Si-Si calibration, the formula $E = a_0 + a_1 X + a_2 \sqrt{X}$ was used for both Si detectors (X being the amplitude of electronic signal). Three isotope lines ^4He , ^9Be , and ^{15}N were selected in the raw experimental

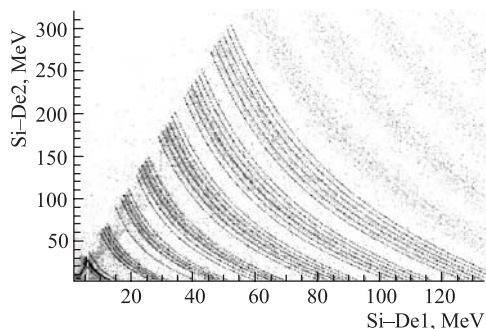


Fig. 4. Calibrated two-dimensional spectrum of Si-Si telescope. The calculated $\Delta E - E$ lines are shown for a wide range of isotopes

spectrum. Additional constraints were applied in the minimization functional in order to position correctly the punch-through points. One can see that the overall agreement in the shape of calculated and calibrated energy losses is very good, both interpolating within and extrapolating beyond the range of selected isotopes (at least to the neighboring element). The way to identification of different isotopes by linearization of experimental spectra and comparison to calculated lines is straightforward.

For Si–CsI(Tl) calibration a similar procedure can be carried out. The difficulty when compared to Si–Si telescope is caused by the fact that the measured signal in CsI(Tl) crystal is the light output which depends on particle energy nonlinearly (including explicit dependence on particle mass and charge). An approximate formula of Tassan–Got [37] for the energy calibration of CsI(Tl) detector can be used

$$E = \sqrt{L^2 + 2\rho L \left(1 + \ln \left(1 + \frac{L}{\rho}\right)\right)}, \quad (4)$$

where L is the light output and $\rho = \eta AZ^2$, where η is a calibration parameter. An example of obtained agreement of experimental and calculated lines is given in Fig. 5 using the data detected in the FAUST array in the reaction $^{40}\text{Ca} + ^{27}\text{Al}$ at $45 A \cdot \text{MeV}$. The calibration of Si detector was obtained using radioactive source of α -particles and the calibration coefficients for CsI(Tl) detector were obtained using a minimization procedure. Due to explicit mass and charge dependence,

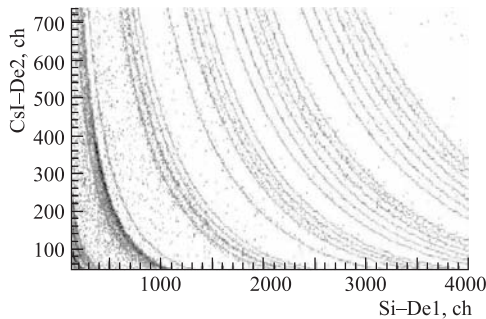


Fig. 5. An example of the raw Si–CsI spectra with decalibrated isotopic dependences of energy losses. The ^4He , ^7Li , and ^9Be lines were used in calibration. The data from reaction $^{40}\text{Ca} + ^{27}\text{Al}$ at $45 A \cdot \text{MeV}$ were collected in ring E of FAUST

the calibration must be preceded by identification, so in this case the calculated $\Delta E - E$ lines are decalibrated using calibration coefficients and projected onto experimental spectrum. Again the overall agreement is quite good both for interpolation and for extrapolation.

The examples of obtained isotope resolution (after linearization) are given in Figs. 6, 7. Data from the reaction $^{124}\text{Sn} + ^{124}\text{Sn}$ at $28 A \cdot \text{MeV}$ were collected

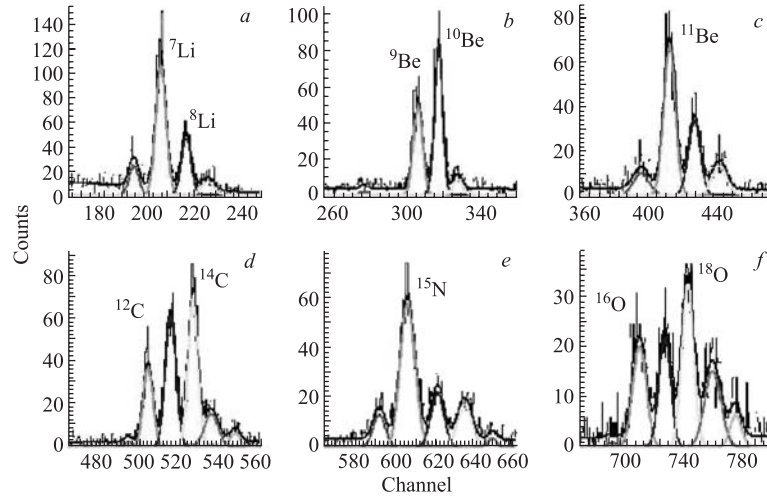


Fig. 6. Isotope resolution obtained after linearization of Si-Si spectra. Data from the reaction $^{124}\text{Sn} + ^{124}\text{Sn}$ at $28 A \cdot \text{MeV}$ were collected in ring 8 of NIMROD [38,39]

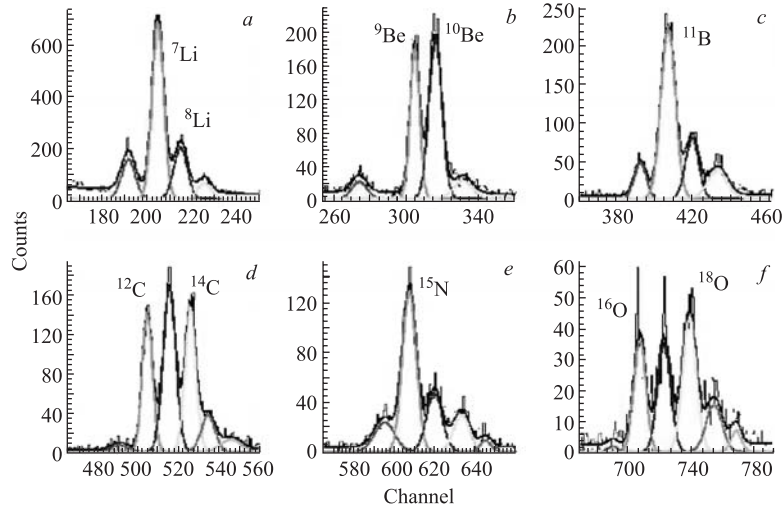


Fig. 7. Isotope resolution obtained after linearization of Si-CsI spectra. Data from the reaction $^{124}\text{Sn} + ^{124}\text{Sn}$ at $28 A \cdot \text{MeV}$ were collected in ring 8 of NIMROD [38,39]

in ring 8 of NIMROD. One isotope line for each Z was used in linearization. The examples of particle spectra calibrated using the above methods are given in Fig. 8. Data used in Fig. 8 were collected in the reaction $^{124}\text{Sn} + ^{28}\text{Si}$ at

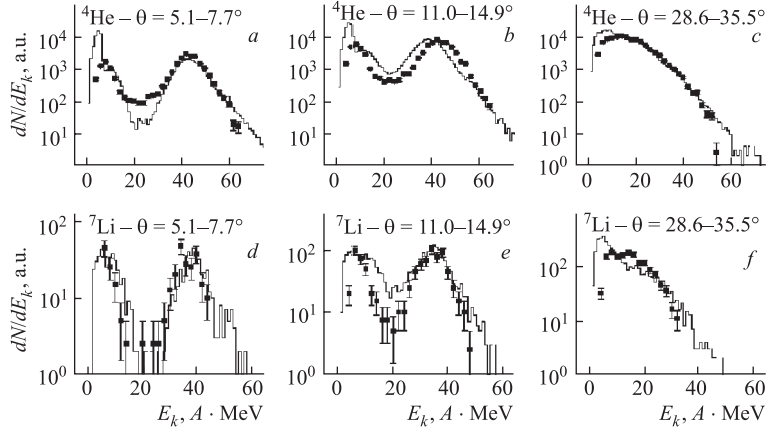


Fig. 8. The experimental particle energy spectra [38] compared to the results of simulations [24]

28 $A \cdot \text{MeV}$ using NIMROD [38,39]. The experimental spectra are compared to simulations [24] described in the previous section.

Event Characterization. Modern multidetector arrays with large angular coverage offer a possibility of studying not only the inclusive observables such as isotope yields and particle spectra but allow one to study development of the fragment properties with evolving reaction dynamics. Typical goal of the exclusive study is to identify dynamical properties of the hot multifragmentation source being created in the early stage of the nucleus–nucleus collision. Here we provide some examples for both peripheral and violent collisions.

Using the forward arrays like FAUST one usually observes the multifragmentation of the hot quasi-projectile which originates from peripheral and midperipheral nucleus–nucleus collision. We present here an example of the projectile multifragmentation in the reaction of ^{28}Si beam with ^{112}Sn and ^{124}Sn targets [10]. A hot multifragmenting source was identified using the calorimetry technique for the events where all emitted fragments were isotopically identified. The velocity distributions of the reconstructed quasi-projectiles with total charge $Z_{\text{tot}} = 12\text{--}15$ were determined. Resulting velocity distributions for the projectile energies 30 and 50 $A \cdot \text{MeV}$ are given in Fig. 9, *a, b*. Solid squares represent the reactions with ^{112}Sn target; and open squares, reactions with ^{124}Sn . For a given projectile energy, the mean velocities and widths of distributions are practically identical for both the targets. The shapes of velocity distributions are close to Gaussian. Velocity distributions are symmetric and no significant low- or high-energy tails are observed. Thus, the reconstructed quasi-projectiles appear to originate from a single source which can be identified with the quasi-projectile.

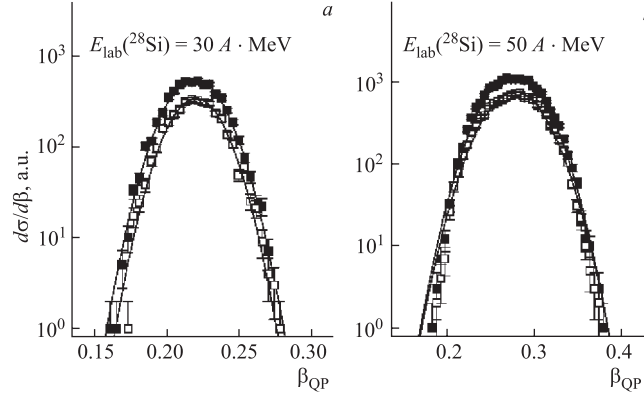


Fig. 9. Experimental velocity distributions of the fully isotopically resolved quasi-projectiles with $Z_{\text{tot}} = 12-15$ [10] (solid and open squares mean ^{112}Sn and ^{124}Sn target, *a* and *b* — the projectile energy 30 and 50 $A \cdot \text{MeV}$, respectively). Solid lines mean Gaussian fits

An apparent charged particle excitation energy of the quasi-projectile can be reconstructed for each projectile fragmentation event from the energy balance in the centre of mass frame of the quasi-projectile

$$E_{\text{app}}^* = \sum_f (T_f^{\text{QP}} + \Delta m_f) - \Delta m_{\text{QP}}, \quad (5)$$

where T_f^{QP} is the kinetic energy of the fragment in the quasi-projectile frame and Δm_f and Δm_{QP} are mass excesses of the fragment and quasi-projectile, respectively. Even if emitted neutrons are not included in this observable, it is useful for the light fragmenting systems, where the neutron emission is not expected to dominate. The distributions of the apparent quasi-projectile excitation energies reconstructed from fully isotopically resolved events are shown in Fig. 10 for both $Z_{\text{tot}} = 14$ and $Z_{\text{tot}} = 12-15$ (solid circles and squares respectively) along with the distributions obtained using DIT/SMM simulation [10] (histograms). The agreement of the simulated and experimental apparent quasi-projectile excitation energy distributions is quite good. The onset of multifragmentation into channels with $Z_f \leq 5$ in the low energy part is described with good precision for all sets of data.

While it is possible to fully reconstruct the projectile-like sources in the mass range $A = 20-30$ in peripheral collisions, with increasing violence of the nucleus–nucleus collision, a hot nucleus is formed from the parts of both the projectile and the target. The excitation energy of such a source is high enough for emission of several intermediate mass fragments (IMF). Information

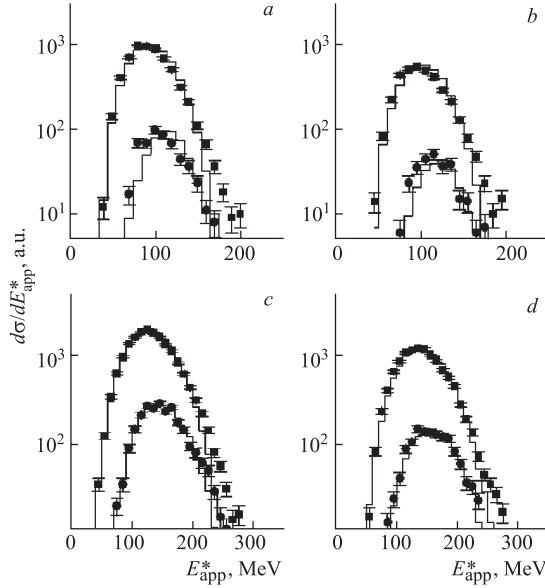


Fig. 10. Distributions of the reconstructed apparent excitation energies of the quasi-projectiles [10]. Symbols mean experimental distributions of the set of fully isotopically resolved quasi-projectiles with $Z_{\text{tot}} = 14$ (●) and $Z_{\text{tot}} = 12-15$ (■). Histograms mean simulated distributions for corresponding data sets: a) ^{28}Si (30 A · MeV) + ^{112}Sn ; b) ^{28}Si (30 A · MeV) + ^{124}Sn ; c) ^{28}Si (50 A · MeV) + ^{112}Sn ; d) ^{28}Si (50 A · MeV) + ^{124}Sn

on both mass and charge of emitted IMFs can be crucial to determine the emission mechanism and thus properties of the emitting source. Various techniques have been developed in order to characterize the impact parameter of the collision (for a detailed study see [40]). A simple method which is nevertheless widely used to determine the centrality of collision is based on the assumption that the particle multiplicity increases monotonously with impact parameter [41]. However, such assumption may be too simplistic, and more sophisticated methods using the combinations of several observables are developed [40]. As an example, we present here a method [38] where the centrality bins are selected in the two-dimensional histogram of IMF multiplicities (M_{IMF}) vs. multiplicities of charged particles (M_{CP}) by parallel lines chosen so that the most central bin integrates the events with the highest multiplicities of charged particles and the highest IMF multiplicities (see Fig. 11, *b*) with the intermediate event classes, thus reflecting the effect of finite size. Figure 11, *a* shows that the shapes of spectra develop with increasing centrality.

Event shape analysis was carried out for two-dimensional M_{IMF} vs. M_{CP} cuts as well as for the one-dimensional M_{IMF} and M_{CP} cuts. All types of centrality cuts exhibit similar trends in terms of sphericity and coplanarity (see Fig. 12), nevertheless some differences can be observed in the most central bins. When considering the total number of events selected by various criteria, the statistics in the most central bin of the two-dimensional selection increased by

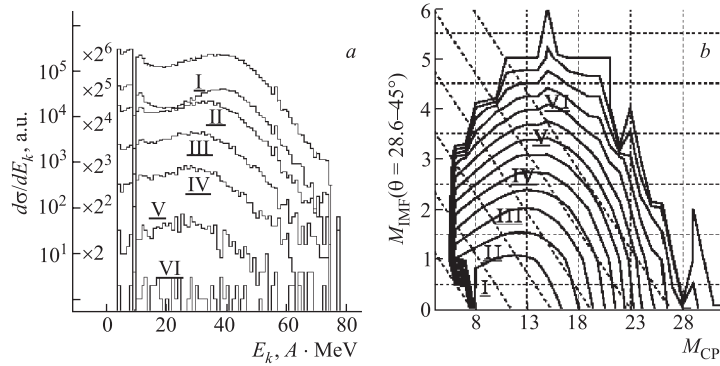


Fig. 11. *a*) Inclusive spectrum of α particles (top) from reaction $^{124}\text{Xe} + ^{124}\text{Sn}$ and spectra for 6 centrality bins ordered from top to bottom by increasing centrality [38]. *b*) Centrality cuts in the M_{IMF} vs. M_{CP} histogram. Skewed lines indicate centrality cuts used in *a*, horizontal and vertical lines indicate one-dimensional cuts in M_{IMF} and M_{CP} histograms

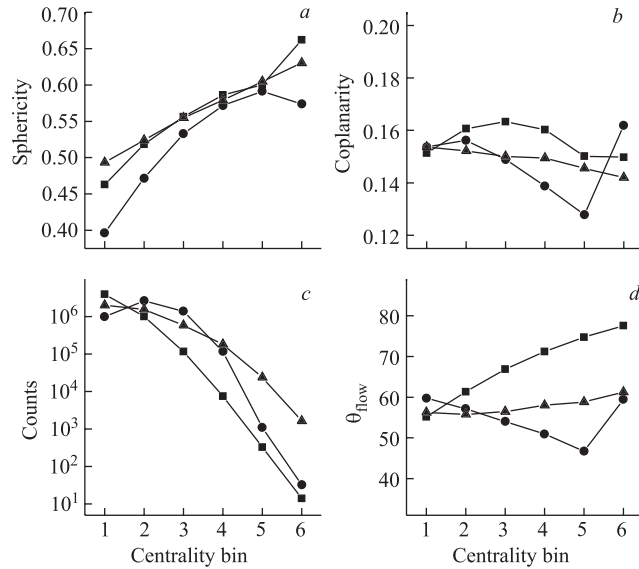


Fig. 12. Test of centrality selections in terms of sphericity (*a*), coplanarity (*b*), event statistics (*c*) and flow angle (*d*) for two-dimensional M_{IMF} vs. M_{CP} cuts (\blacktriangle) as well as for the one-dimensional M_{IMF} (\blacksquare) and M_{CP} (\bullet) cuts [38]

two orders of magnitude compared to the traditional M_{CP} selection (see Fig. 12). Such a gain in statistics is caused by better separation of central and peripheral events. The one-dimensional cuts typically admix high-multiplicity peripheral

events to a smaller number of genuine central events, thus decreasing the overall centrality. The use of two-dimensional criteria allows more detailed studies of central events.

ISOTOPIC TRENDS

The isotopic composition of the multifragmentation products such as light charged particles (LCP), intermediate mass fragments (IMF) and heavy residues is an experimental information which can be used to trace the dynamics of isospin degrees of freedom during the multifragmentation and, using grand-canonical picture, to extract the values of thermodynamical observables of the system undergoing multifragmentation such as temperature and free nucleon densities. The isotopic composition can be studied both as a bulk or in terms of yield ratios of specific isotopes. Variation of the neutron content of reaction products can be used to characterize the response of the isotopic composition to variation of initial conditions.

Isotopic Distributions. A wide variety of fragment species is typically produced in multifragmentation of heavy nuclei. In order to obtain information on isospin dynamics, an obvious choice is to study the behavior of isotopic chains. As an example we provide in Fig. 13 isotopic distributions of fragments with $Z = 2-8$ from four reactions of ^{124}Sn , ^{124}Xe beams with $^{112,124}\text{Sn}$ targets at $28 A \cdot \text{MeV}$ [38,39] studied at the Cyclotron Institute of Texas A&M University using the 4π multidetector array NIMROD [35]. The isotopic distributions from different reactions are distinguished by different symbols. Each panel shows the isotopic distributions measured at three angular ranges corresponding to rings 2, 5 and 8 (from top to bottom).

As one can see, the overall shapes remain quite similar at different angular ranges. It is interesting to note that the isotopes with maximum yield for $Z \geq 3$ are typically those with $A = 2Z + 1$ for both even and odd Z . The effect of different reactions is most pronounced at the proton and neutron-rich tails of distributions, neutron-rich isotopes being more abundant in neutron-rich systems and vice versa, while the central part corresponding to β -stable nuclei is relatively insensitive. In any case, such comparisons of the shapes of isotopic distributions are rather qualitative. A quantitative analysis can be carried out in terms of integral observables such as momenta of distributions.

To express the effect of experimental conditions such as projectile-target combination or detection angle quantitatively one can evaluate the mean N/Z - (neutron to proton) ratio for each isotopic chain. In Fig. 14 there are given the mean N/Z -ratios of emitted fragments with $Z = 2-8$ from four reactions obtained at different angles [38]. The overall dependence is similar at all angular ranges. He-isotopes are dominated by α particles. Mean N/Z ratios are the

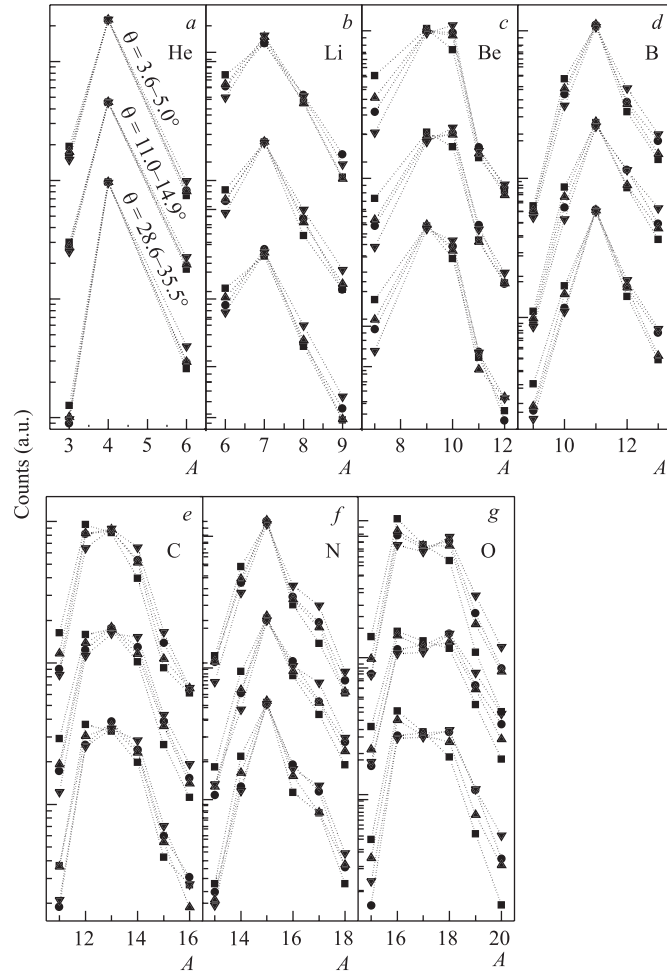


Fig. 13. Isotopic distributions of fragments with $Z = 2-8$ from four reactions of ^{124}Sn , ^{124}Xe beams with $^{112,124}\text{Sn}$ targets at $28 A \cdot \text{MeV}$ [38, 39], measured using the 4π multidetector array NIMROD [35] at three angular ranges: \blacksquare — $^{124}\text{Xe} + ^{112}\text{Sn}$; \bullet — $^{124}\text{Xe} + ^{124}\text{Sn}$; \blacktriangle — $^{124}\text{Sn} + ^{112}\text{Sn}$; \blacktriangledown — $^{124}\text{Sn} + ^{124}\text{Sn}$

highest for Li and Be isotopes and decrease gradually with increasing atomic number of IMFs. When comparing mean N/Z ratios from four reactions, two characteristic patterns can be distinguished. At most forward angles the mean N/Z ratios of Li and Be isotopes appear to track with the isospin asymmetry of the composite projectile-target system what leads to grouping of experi-

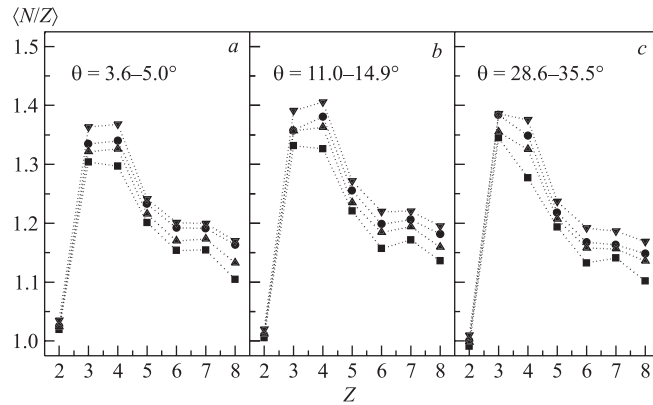


Fig. 14. Mean N/Z -ratios of emitted fragments with $Z = 2-8$ from four reactions obtained at different angles [38, 39]: ■ — $^{124}\text{Xe} + ^{112}\text{Sn}$; ● — $^{124}\text{Xe} + ^{124}\text{Sn}$; ▲ — $^{124}\text{Sn} + ^{112}\text{Sn}$; ▼ — $^{124}\text{Sn} + ^{124}\text{Sn}$

mental points from four reactions into a typical 1-2-1 pattern (representing reactions $^{124}\text{Sn} + ^{124}\text{Sn} - ^{124}\text{Sn} + ^{112}\text{Sn}$ and $^{124}\text{Xe} + ^{124}\text{Sn} - ^{124}\text{Xe} + ^{112}\text{Sn}$, respectively). On the other hand, the isotopes with $Z = 5-8$ appear to track with the isospin asymmetry of the target nucleus what creates a 2-2 pattern (representing reactions $^{124}\text{Sn} + ^{124}\text{Sn}$ and $^{124}\text{Xe} + ^{124}\text{Sn} - ^{124}\text{Sn} + ^{112}\text{Sn}$ and $^{124}\text{Xe} + ^{112}\text{Sn}$, respectively). At angles $11.0-14.9^\circ$ the 1-2-1 pattern can be identified for Li and Be isotopes while for heavier fragments the patterns vary. At angles $28.6-35.5^\circ$ one can recognize the 2-2 pattern for Li isotopes while at heavier fragments the 1-2-1 pattern dominates. In principle, one can identify the 1-2-1 pattern with the fragments emitted from a hot composite source and 2-2 pattern to the emission from a quasi-projectile. The fragments with $Z = 5-8$ at forward angles possibly originate from the binary de-excitation channels of the quasi-projectile while the 2-2 pattern of Li isotopes at the most central angles suggests either backward emission from the quasi-projectile or emission from quasi-target. Similar isospin asymmetry patterns can be identified also in the isotopic yield distributions in Fig. 13. Thus, the mean values of N/Z ratio appear to exhibit an interesting information on isospin dynamics. The relative variation of the mean N/Z values is nevertheless rather small when compared to the variation of isospin-asymmetry of the projectile-target combination and more sensitive isospin tracers should be identified.

Yield Ratios. As demonstrated in the previous subsection, variation of the projectile and target nuclei influences the integral characteristics of isotopic distributions, such as mean values of N/Z ratio, rather weakly. Nevertheless, when observing the evolution of isotopic distributions in different reactions and

angular ranges, one can notice that the relative yields of neighboring isotopes are rather sensitive (especially at the tails of distributions). Such yield ratios have been widely used in experimental studies of multifragmentation data for last 15 years [42].

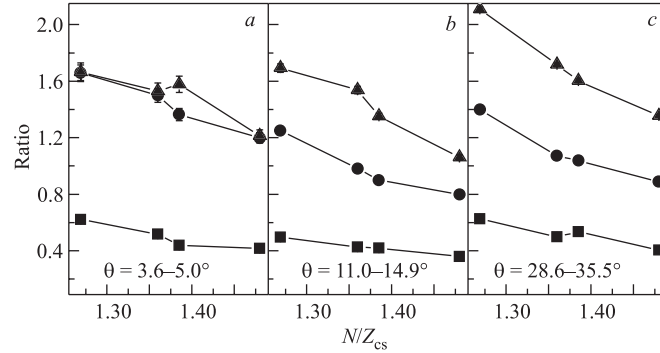


Fig. 15. Three isotopic yield ratios for the multifragmentation data from four reactions of ^{124}Sn , ^{124}Xe beams with $^{112,124}\text{Sn}$ targets at $28 A \cdot \text{MeV}$ [38, 39] at three different angular ranges. The data from different reactions are characterized by a N/Z ratio of the composite system (N/Z_{cs}): ■ — $^6\text{Li}/^7\text{Li}$; ● — $^9\text{Be}/^{10}\text{Be}$; ▲ — $^{13}\text{C}/^{14}\text{C}$

As an example, we present in Fig. 15 the values of three isotopic yield ratios, again for the multifragmentation data [38, 39] from four reactions of ^{124}Sn , ^{124}Xe beams with $^{112,124}\text{Sn}$ at $28 A \cdot \text{MeV}$. In most cases one can observe an approximately exponential dependence of the isotopic yield ratio on the N/Z ratio of the composite system (N/Z_{cs}), which can be expected according to formula (1) when assuming linear dependence of the neutron chemical potential on N/Z_{cs} . The yield ratios depend rather strongly on the angular range. Such a dependence can be caused by different isospin dynamics at different angles.

Furthermore, we present in Fig. 16 the values of three isobaric yield ratios for the same multifragmentation data. Specifically, the isobaric ratios are evaluated for pairs of mirror nuclei. The sensitivity of isobaric ratios to N/Z_{cs} is significantly stronger than in the previous case, especially for the ratios $^9\text{Be}/^9\text{B}$ and $^{11}\text{B}/^{11}\text{C}$, where the fragments ^9B and ^{11}C are populated rather weakly. The overall behavior is nevertheless rather irregular. Especially the observed pattern at most forward angles suggests a contribution from the cold process such as projectile break-up, which appears to contribute considerably to production of isospin-asymmetric species at forward angles. Such observation is in agreement with available experimental data [43].

A behavior of the yield ratio of mirror nuclei $^3\text{H}/^3\text{He}$ was investigated in the quasi-projectile multifragmentation of a ^{28}Si beam with ^{112}Sn and ^{124}Sn targets

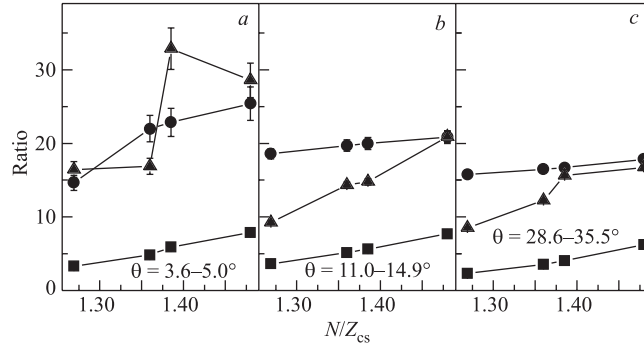


Fig. 16. Three isobaric yield ratios for the multifragmentation data from four reactions of ^{124}Sn , ^{124}Xe beams with $^{112,124}\text{Sn}$ targets at $28 A \cdot \text{MeV}$ [38,39] at three different angular ranges. The data from different reactions are characterized by a N/Z ratio of the composite system (N/Z_{CS}): ■ — $^7\text{Li}/^7\text{Be}$; ● — $^9\text{Be}/^9\text{B}$; ▲ — $^{11}\text{B}/^{11}\text{C}$

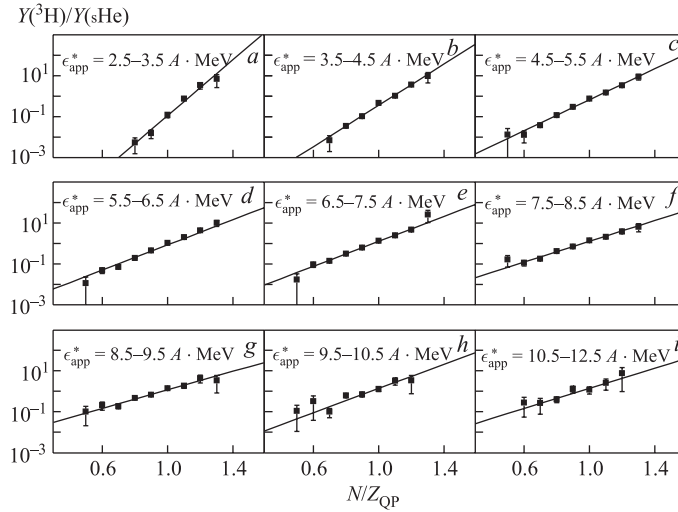


Fig. 17. Dependence of the yield ratio $Y(^3\text{H})/Y(^3\text{He})$ on N/Z ratio of the isotopically resolved quasi-projectiles with $Z_{\text{QP}} = 12-15$ for nine bins of ϵ_{app}^* [44]

at 30 and $50 A \cdot \text{MeV}$ [44]. As described in experimental section, the properties of the system which actually undergoes multifragmentation, including N/Z ratio (N/Z_{QP}), are known with good precision. Figure 17 shows the dependence of the isobaric yield ratio $Y(^3\text{H})/Y(^3\text{He})$ on N/Z_{QP} for nine bins of the apparent excitation energy per mass unit of the quasi-projectile (ϵ_{app}^*). The experimental

data are represented as squares and the lines represent the exponential fits. The observed exponential dependence in all excitation energy bins is in agreement with formula (1). The slopes are the steepest at low excitation energies and become flatter with increasing excitation energy.

The apparent compliance of the yield ratio behavior to the grand-canonical picture as represented by formula (1) suggests the possibility to extract the values of thermodynamic observables, in particular temperature. The procedure for extraction of the temperature was suggested by Albergo [45]. When expressing the isotopic yield within the equilibrium limit of the grand-canonical ensemble, a simplified analogue of formula (1) is obtained [46]

$$Y(N, Z) = F(V, T)g(N, Z) \exp((1/T)(B(N, Z) + N\mu_n + Z\mu_p)). \quad (6)$$

The isotopic yield is thus essentially governed by free neutron and proton chemical potentials $\mu_{n,p}$, temperature T , and fragment binding energy $B(N, Z)$. The factor $F(V, T)$ encompasses information on the global properties of the fragment partition. The ground state spin degeneracy factor $g(N, Z)$ represents the internal state sum of the fragment, which is restricted to a ground state only. In order to extract temperature, a double isotope ratio is constructed [45]

$$\frac{Y(N_1 + 1, Z_1)/Y(N_1, Z_1)}{Y(N_2 + 1, Z_2)/Y(N_2, Z_2)} = \frac{g(N_1 + 1, Z_1)/g(N_1, Z_1)}{g(N_2 + 1, Z_2)/g(N_2, Z_2)} \times \exp\left(\frac{B(N_1 + 1, Z_1) - B(N_1, Z_1) - B(N_2 + 1, Z_2) + B(N_2, Z_2)}{T}\right) \quad (7)$$

and the temperature T can be obtained as

$$T = \frac{\Delta B_{1234}}{\ln a \frac{Y(N_1 + 1, Z_1)/Y(N_1, Z_1)}{Y(N_2 + 1, Z_2)/Y(N_2, Z_2)}}, \quad (8)$$

where $a = \frac{g(N_2 + 1, Z_2)/g(N_2, Z_2)}{g(N_1 + 1, Z_1)/g(N_1, Z_1)}$ and $\Delta B_{1234} = B(N_1 + 1, Z_1) - B(N_1, Z_1) - B(N_2 + 1, Z_2) + B(N_2, Z_2)$. Thus an estimate of the grand-canonical temperature can be determined using the isotope yields and some of their ground state characteristics.

Formula (8) was used extensively in experimental studies during the last decade [27, 47]. Typically, the temperature determined using various thermometers (sets of isotope yields) exhibited large spread, possibly due to side-feeding from secondary decay. A method of correction for the secondary decay was proposed by Tsang et al. [48]. In [38] we employed a graphical method to extract the average temperature. The isotopic yield ratios, corrected for the ground state

spin degeneracy, are plotted as a function of the binding energy difference (see Fig. 18). The data from four reactions of ^{124}Sn , ^{124}Xe beams with $^{112,124}\text{Sn}$ targets at $28 A \cdot \text{MeV}$, used already in Figs. 15, 16, are investigated. Individual double isotope ratio thermometers can be represented (in the logarithmic scale) when connecting the two points corresponding to the used isotope ratios by a

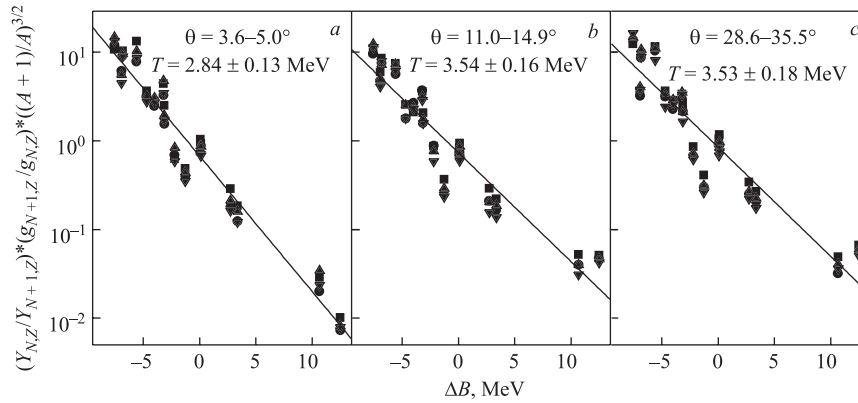


Fig. 18. Systematics of corrected isotopic ratios $Y_{N,Z}/Y_{N+1,Z}$ from four reactions plotted against the difference of binding energies [38]: \blacksquare — $^{124}\text{Xe} + ^{112}\text{Sn}$; \bullet — $^{124}\text{Xe} + ^{124}\text{Sn}$; \blacktriangle — $^{124}\text{Sn} + ^{112}\text{Sn}$; \blacktriangledown — $^{124}\text{Sn} + ^{124}\text{Sn}$

straight line. The inverse of the slope of such line is then the temperature. When assuming that the effect of side-feeding in the secondary decay is distributed randomly, an average temperature can be obtained by a linear fit of the systematics of all isotopic yield ratios.

Information on the temperature can be obtained also from the slope of dependence of the isobaric yield ratio $Y(^3\text{H})/Y(^3\text{He})$ on neutron-to-proton ratio of the quasi-projectile N/Z_{QP} . The data from reactions of a ^{28}Si beam with ^{112}Sn and ^{124}Sn targets at 30 and 50 $A \cdot \text{MeV}$ (see Fig. 17) were used [44] and the extracted temperatures compared well with the temperatures obtained using the double isotope ratio thermometer $(^2\text{H}/^3\text{H})/(^3\text{He}/^4\text{He})$. An assumption was employed that the values of chemical potentials can be approximated by the values of separation energies. The reason why such approximation is applicable for a hot expanded nucleus can be in the possible interplay of the effect of expansion (reducing absolute values of chemical potentials) and separation of the isospin-asymmetric free nucleon gas from the isospin-symmetric heavier liquid phase [44], as indicated by observed inhomogeneous isospin distribution among light charged particles and heavier fragments [49].

The isotopic yield can be, within the equilibrium limit of the grand-canonical ensemble, expressed in terms of the density of the free nucleon gas [45,46]

$$Y(N, Z) \propto V \rho_n^N \rho_p^Z g(N, Z) \exp(B(N, Z)/T), \quad (9)$$

where $\rho_{n,p} \propto \exp(\mu_{n,p}/T)$. The values of yield ratios of mirror nuclei with $N - Z = 1$ can be expressed then as

$$\frac{Y(N, Z)}{Y(Z, N)} \simeq \frac{g(N, Z)}{g(Z, N)} \frac{\rho_n}{\rho_p} \exp(\Delta B/T) \quad (10)$$

thus relating the yield ratio to the density ratio of the free neutron and proton gas. The yield ratios of the mirror nuclei ${}^3\text{H}/{}^3\text{He}$, ${}^7\text{Li}/{}^7\text{Be}$, and ${}^{11}\text{B}/{}^{11}\text{C}$ were used in work [50] to determine the ratio ρ_n/ρ_p by an exponential extrapolation toward $\Delta B = 0$, yielding the values approximately 2–5. While such approximation is valid for grand-canonical ensemble of infinite systems, when dealing with the finite systems such as nuclei, the values of free nucleon chemical potentials depend on the fragment partition in a way guaranteeing conservation of the mass and charge of the system. Thus the value of the ratio ρ_n/ρ_p may differ strongly for different event classes and no globally applicable value may exist in the finite system. Furthermore, the effect of secondary emission may also contribute to uncertainty in determination of ρ_n/ρ_p .

Isoscaling. As shown in the previous subsection, the fragment yield ratios can be used to extract thermodynamical observables of the fragmenting system such as temperature and chemical potential. In the context of isotopic distributions, the fragment yield ratios represent the details of the distribution sensitive to isospin degrees of freedom. Similar sensitivity can be explored globally by investigating the ratio of isotopic yields from two processes with different isospin asymmetry, essentially dividing the two isotopic distributions in point-by-point fashion. When employing the formula (6), such a ratio will depend on N and Z as follows [51]

$$R_{21}(N, Z) = Y_2(N, Z)/Y_1(N, Z) = C \exp(\alpha N + \beta Z), \quad (11)$$

where $\alpha = \Delta\mu_n/T$ and $\beta = \Delta\mu_p/T$, $\Delta\mu_n$ and $\Delta\mu_p$ are the differences in the free neutron and proton chemical potentials of the fragmenting systems. C is an overall normalization constant. Alternatively [52], the dependence can be expressed as

$$R_{21}(N, Z) = Y_2(N, Z)/Y_1(N, Z) = C \exp(\alpha' A + \beta'(N - Z)) \quad (12)$$

thus introducing the parameters which can be related to the isoscalar and isovector components of free nucleon chemical potential since $\alpha' = \Delta(\mu_n + \mu_p)/2T$ and $\beta' = \Delta(\mu_n - \mu_p)/2T$.

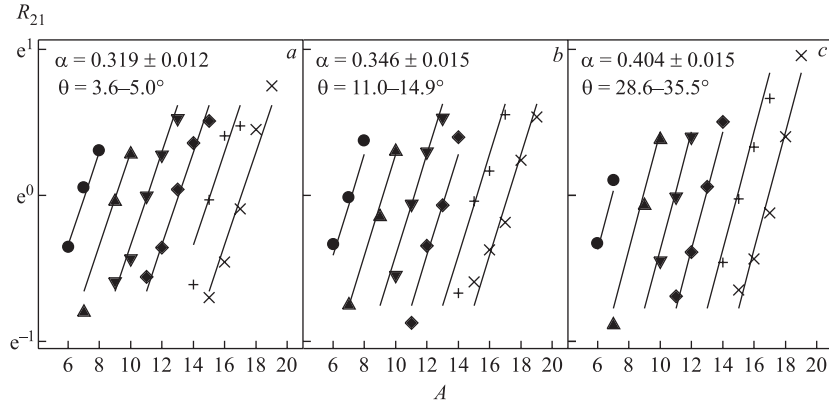


Fig. 19. The isoscaling plots for the multifragmentation data from reactions of $^{124}\text{Sn} + ^{124}\text{Sn}$ and $^{124}\text{Xe} + ^{112}\text{Sn}$ at $28 A \cdot \text{MeV}$ [38,39] at three different angular ranges: ● — Li; ▲ — Be; ▼ — B; ◆ — C; + — N; × — O

An exponential scaling of R_{21} with the isotope neutron and proton numbers was observed experimentally in the multifragmentation data from the reactions of high-energy light particle with massive target nucleus [52,53] or from the reactions of mass symmetric projectile and target at intermediate energies [51] and such behavior is called isoscaling [51] (the parameters $\alpha, \beta, \alpha', \beta'$ being called isoscaling parameters). Isoscaling behavior was further reported in heavy residue data [54] and also in fission data [55]. It was shown that the values of isoscaling parameters can be related to symmetry energy [51,52], to the level of isospin equilibration [54] and to the values of transport coefficients [55]. An example of isoscaling behavior of the fragments with $Z = 3-8$ detected in the reactions of $^{124}\text{Sn} + ^{124}\text{Sn}$ and $^{124}\text{Xe} + ^{112}\text{Sn}$ at $28 A \cdot \text{MeV}$ [38,39] is given in Fig. 19. The isoscaling behavior is rather regular at all three angular ranges, the isoscaling parameter α increases with the detection angle. Such a trend of the isoscaling parameter α can be possibly related to the fact that with increasing angle the fragments originate from still more damped collisions, with increasing level of isospin equilibration between projectile- and target-like fragment [56].

In Fig. 20, there are presented the isoscaling data from a statistical decay of hot quasi-projectiles from the reactions $^{28}\text{Si} + ^{124,112}\text{Sn}$ at projectile energy $50 A \cdot \text{MeV}$ [57]. Observed charged particles with $Z \leq 5$ were isotopically resolved and total observed charge was close to the charge of the projectile ($Z = 12-15$) [10,58]. Due to the restricted set of identified fragment species, the isoscaling plots are presented, according to formula (12), as a function of isospin asymmetry. The isoscaling plots are presented not only for the full data but also for five bins of excitation energy. The slopes depend on the excitation energy in

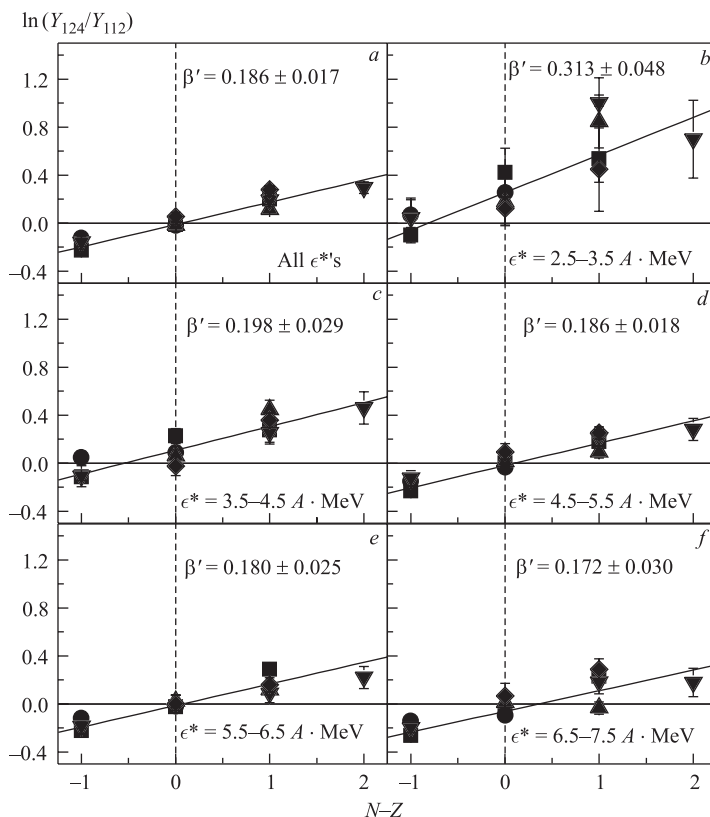


Fig. 20. The isoscaling plots from the reactions of $^{28}\text{Si} + ^{124,112}\text{Sn}$ at $50 A \cdot \text{MeV}$ for the full set of isotopically resolved quasi-projectiles (a) and for five bins of quasi-projectile excitation energy per nucleon [57] (b-f): \blacksquare — H; \bullet — He; \blacktriangle — Li; \blacktriangledown — Be; \blacklozenge — B

a similar way as the slope of the dependence of isobaric ratio $Y(^3\text{H})/Y(^3\text{He})$ on the quasi-projectile N/Z observed in [44] (see Fig. 17). When compared to similar results at $30 A \cdot \text{MeV}$, the isoscaling parameters β' for individual excitation energy bins do not depend on the projectile energy and the difference of the slopes of the inclusive data is caused by different excitation energy distributions of the hot quasi-projectiles at two projectile energies (see Fig. 10).

As demonstrated, isoscaling appears to be a global feature of the multifragmentation data and the values of isoscaling parameters show sensitivity to properties of the hot source. It is of interest to explore such a sensitivity in the studies of thermodynamical properties of the multifragmenting source.

THERMODYNAMICAL PROPERTIES OF THE HOT QUASI-PROJECTILES

In the previous section we presented an overview of the methods by which the isotopic trends of the fragment data can be used to extract thermodynamical observables of the hot multifragmenting source. Here we present a systematic investigation of thermodynamical properties of the well-characterized hot quasi-projectiles with masses $A = 20-30$, originating from the reactions $^{28}\text{Si} + ^{124,112}\text{Sn}$ at the projectile energy of 30 and 50 $A \cdot \text{MeV}$ [10]. Signatures and argumentation supporting the conclusion that multifragmentation of such quasi-projectiles is a statistical process will be presented. Furthermore, the signals for the isospin-asymmetric liquid-gas phase transition in the nuclear matter as a process underlying to multifragmentation will be investigated and implications for the nuclear equation of state at subsaturation densities will be discussed.

Production Mechanism and Equilibrium. In order to establish whether the fragment data from reactions $^{28}\text{Si} + ^{124,112}\text{Sn}$ at projectile energy of 50 and 30 $A \cdot \text{MeV}$ [10] originate from statistical decay of hot quasi-projectiles, it is necessary to investigate the dynamical properties of the projectile-like source and to determine the production mechanism. The observed fragment data [10, 58] provide full information (with the exception of emitted neutrons) on the decay of thermally equilibrated hot quasi-projectiles with known mass ($A = 20-30$), charge, velocity, and excitation energy. The detailed investigation of the reaction mechanism [10] allowed one to establish a dominant reaction scenario. The excellent description of the fragment observables was obtained using the model of deep-inelastic transfer (DIT) [59] for the early stage of collisions and the statistical multifragmentation model (SMM) [5] for de-excitation. The model describes well the dynamical properties of the reconstructed quasi-projectile such as centre-of-mass velocity, excitation energy (see Fig. 10), and isospin-asymmetry (see Fig. 21). The fragment observables such as multiplicity, charge distributions, and mean values of N/Z for a given charge were also reproduced reasonably well [10]. Thus the data can be considered as well understood in terms of reaction mechanism.

The observation that a wide range of observables is in agreement with the dominant reaction scenario of the deep inelastic transfer (binary collision with intense nucleon exchange between the projectile and target nuclei, each of them represented by a statistically equilibrated Fermi gas) followed by statistical multifragmentation (assuming statistically equilibrated freeze-out configuration) allows one to conclude that the assumption of statistical equilibrium is applicable and that thermodynamical observables can be defined for the hot quasi-projectile. The experimentally observed exponential scaling behavior shown in Figs. 17 and 20 further demonstrates compliance with grand-canonical picture. The contribution from nonequilibrium processes such as pre-equilibrium emission was shown to be

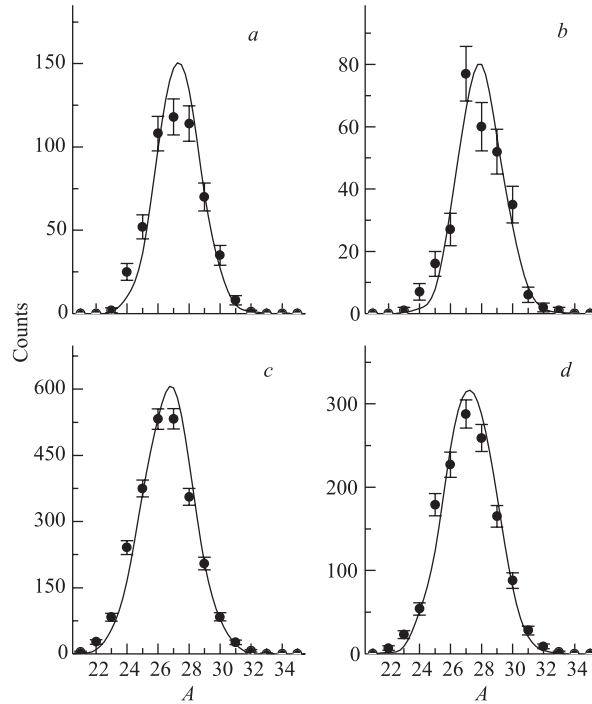


Fig. 21. Experimental (●) and simulated (solid lines) mass distributions for the fully isotopically resolved quasi-projectiles with $Z_{\text{tot}} = 14$ [10]: *a*) ^{28}Si ($30 A \cdot \text{MeV}$) + ^{112}Sn ; *b*) ^{28}Si ($30 A \cdot \text{MeV}$) + ^{124}Sn ; *c*) ^{28}Si ($50 A \cdot \text{MeV}$) + ^{112}Sn ; *d*) ^{28}Si ($50 A \cdot \text{MeV}$) + ^{124}Sn

weak [10]. The number of emitted neutrons, which are not detected, is, according to successful DIT/SMM simulation, between one and two per event (0.9 and 1.2 for ^{112}Sn and ^{124}Sn at $30 A \cdot \text{MeV}$ and 1.4 and 1.7 at $50 A \cdot \text{MeV}$ [10], respectively) and the underestimation of the excitation energy by the evaluated apparent excitation energy due to neutron emission can be expected approximately 10–15% in a wide range of excitation energies. The shapes of the dependences of experimental observables on excitation energy thus will not be affected dramatically. To summarize this subsection, the observed quasi-projectile multifragmentation data offer a good opportunity for investigation of thermodynamical properties of the multifragmentation source and of the possible phase transition.

Thermodynamical Observables and Isospin-Asymmetric Phase Transition.

In order to investigate thermodynamical properties of the hot multifragmentation source, one needs to characterize a set of observables, including extensive ones such as thermal excitation energy (heat) and intensive ones such as temperature and chemical potentials.

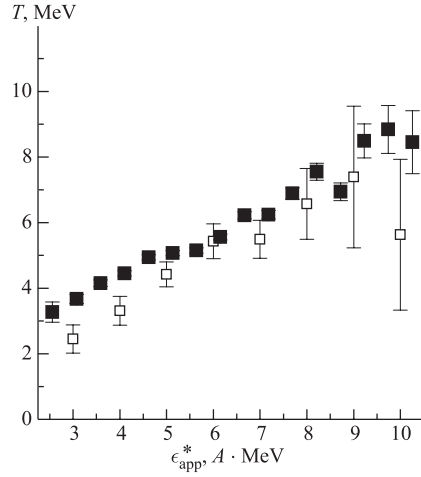


Fig. 22. Dependence of the temperature T on excitation energy ϵ_{app}^* . ■ — temperature determined using the double isotope ratio thermometer $d, t/{}^3\text{He}, {}^4\text{He}$; □ — temperature determined from the dependence of the yield ratio $Y({}^3\text{H})/Y({}^3\text{He})$ on the N/Z ratio of the quasi-projectile [44]

For the quasi-projectile data from the reactions ${}^{28}\text{Si} + {}^{124,112}\text{Sn}$ at projectile energy of 30 and 50 $A \cdot \text{MeV}$, temperature was determined both using double isotope ratio method and the N/Z dependence of the isobaric yield ratio $Y({}^3\text{H})/Y({}^3\text{He})$ [44]. The results are shown in Fig. 22. Both methods seem to provide consistent results. Double isotope ratio temperature appears to exhibit a short plateau starting around $\epsilon_{\text{app}}^* = 4.5 A \cdot \text{MeV}$, while for the $Y({}^3\text{H})/Y({}^3\text{He})$ temperature, due to larger statistical errors, only a hint of similar feature can be identified at somewhat higher excitation energy. The presence of a plateau in the caloric curve was interpreted in the literature [60] as a signature of the first-order phase transition, nevertheless the influence of additional effects such as nonthermal flow or variation of the source size may affect the shape of the observed caloric curve [61] and such a signal cannot be considered

as an unambiguous signature without providing further evidence. For the data in Fig. 22 the influence of nonthermal flow and variation of the source size can be excluded due to well understood reaction mechanism.

Of the two methods for temperature determination, the $Y({}^3\text{H})/Y({}^3\text{He})$ temperature relies on additional assumption concerning chemical potentials. The insight into behavior of the chemical potentials can be obtained using the isoscaling analysis. The values of the isoscaling parameter β' for the data in Fig. 20 can be related, according to formula (12), to the isovector component of the chemical potential. In Fig. 23, *a* we present an estimate of the difference of isovector chemical potential using the observable $\beta'T$, canceling out a trivial $1/T$ dependence of the isoscaling parameter [57]. The double isotope ratio temperature [45] from the isotopic ratios $Y({}^2\text{H})/Y({}^3\text{H})$ and $Y({}^3\text{He})/Y({}^4\text{He})$, which is independent of assumptions concerning chemical potentials, was used. The horizontal line represents an estimate of the zero temperature value of $\Delta(\mu_n - \mu_p)$ by the proton and neutron separation energies ($\mu_{p,n} \approx -S_{p,n}$) of reconstructed quasi-projectiles, using the known N/Z equilibration and the correction for neutron emission from back-tracing of DIT/SMM simulations [10]. The zero temperature estimates of $\Delta(\mu_n - \mu_p)$ for subsets of data in all excitation energy bins are consistent with

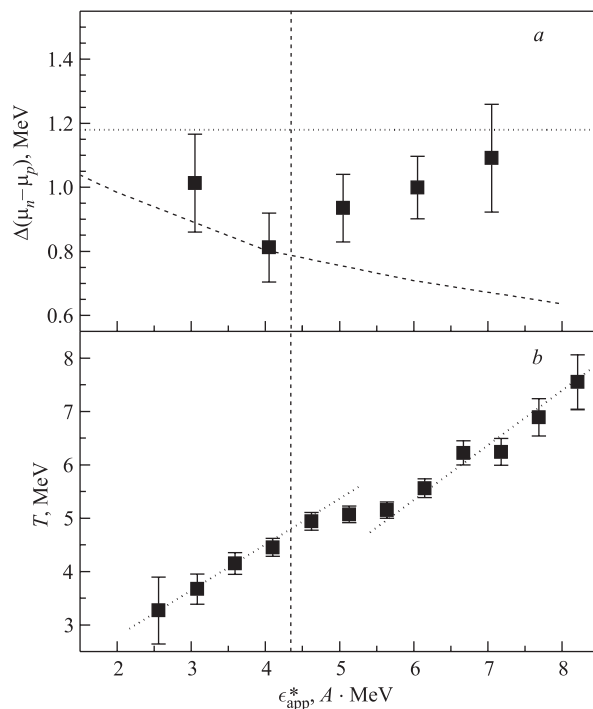


Fig. 23. *a*) The dependence of observable $\beta'T (= \Delta(\mu_n - \mu_p))$ on relative excitation energy of the quasi-projectile [57] (■). Horizontal line shows estimate of $\beta'T$ obtained when assuming $\mu_{p,n} \approx -S_{p,n}$. Dashed curve represents the expected trend for homogeneous system. *b*) Corresponding caloric curve [44]. Vertical line indicates the position of turning point

the horizontal line. Any experimental deviations from the horizontal line can be understood as a nontrivial dependence representing the details of de-excitation. The experimental dependence of $\beta'T$ indicates initial decrease at low excitation energies (consistent with expansion of the homogeneous hot source represented by dashed curve), further it exhibits a turning-point at $4 A \cdot \text{MeV}$ beyond which it increasingly deviates from the trend of the homogeneous (single phase) system, and at apparent excitation energies $6-7 A \cdot \text{MeV}$ the $\beta'T$ value approaches the zero temperature value again. The estimate of $\beta'T$ for homogeneous system (dashed curve) was obtained assuming the Fermi-gas $\rho^{2/3}$ dependence and using the estimate of free volume by formula (2) for each excitation energy bin. The trend explains a reasonable success of the $\mu_{p,n} \approx -S_{p,n}$ approximation used to extract the mirror nucleus temperature in Fig. 22, where the viability of the approximation at high temperatures was supported by a possible counterbalance

of two effects, namely expansion of the hot nucleus (leading to a decrease of the absolute values of chemical potentials) and chemical separation into an isospin symmetric heavy fraction and an isospin asymmetric nucleon gas, leading to the increase of $\mu_n - \mu_p$ of the dilute phase (nucleon gas). Since the isoscaling parameter depends directly on the free nucleon chemical potentials, the turning-point at $4 A \cdot \text{MeV}$ can be understood as a signal of the onset of chemical separation which causes the deviation of the free nucleon chemical potential from the dependence consistent with expansion of the homogeneous system. As demonstrated by comparison with the caloric curve in Fig. 23, *b* (obtained using double isotope ratio thermometer without assumption concerning chemical potentials) the onset of chemical separation is correlated to the onset of the plateau in the caloric curve, thus signaling that chemical separation is accompanied by latent heat. Such a behavior can be expected in the first-order phase transition. The dotted lines in Fig. 23, *b* indicate the discontinuity in the heat capacity of the system.

The behavior, observed in Fig. 23, is consistent with the first-order phase transition. Several signals of the first-order phase transition have been reported in the recent experimental studies, such as negative microcanonical heat capacity [62], characterized by abnormal kinetic energy fluctuation, and the «fossil» signal of spinodal decomposition [63], characterized by abnormal production of equally sized fragments. These indications of the first-order phase transition are based on careful event-by-event analysis of the multifragmentation data combined with model assumptions and results of theoretical simulations. The isospin-asymmetry of the fragments is not explored in such analyses. The behavior shown in Fig. 23 relates the signal of chemical separation to the plateau of the caloric curve, thus providing a signal of isospin-asymmetric first-order phase transition. Further support for such conclusion can be deduced from Fig. 24, *b*, demonstrating the inhomogeneous distribution of isospin-asymmetry [49] among dense and dilute phases represented by light charged particles and intermediate mass fragments, respectively. The effect strongly depends on the N/Z ratio of the quasi-projectile. So are multiplicities of LCPs and IMFs in Fig. 24, *a* which further indicate that with increasing isospin-asymmetry of the quasi-projectile, the dilute phase becomes more isospin-asymmetric and abundant. The observations related to Figs. 23, 24 are consistent with theoretical predictions of the isospin-asymmetric phase transition in nuclear media. The estimated density of the homogeneous system at the turning point in Fig. 23, *a* is consistent with theoretical estimates of the position and shape of the spinodal contour, typically at almost constant total density $0.6\rho_0$ in a wide range of asymmetries [7]. Thus, inside the spinodal region, the homogeneous nuclear medium is quickly replaced by both isospin and spatially inhomogeneous system. Such a conclusion is further supported by a comparison of the temperature obtained using the double isotope ratio thermometer d , $t/{}^3\text{He}$, ${}^4\text{He}$ [44] with kinematic temperatures of p , d , t , ${}^3\text{He}$, ${}^4\text{He}$ obtained from Maxwellian fits of the particle kinetic energy spectra in the

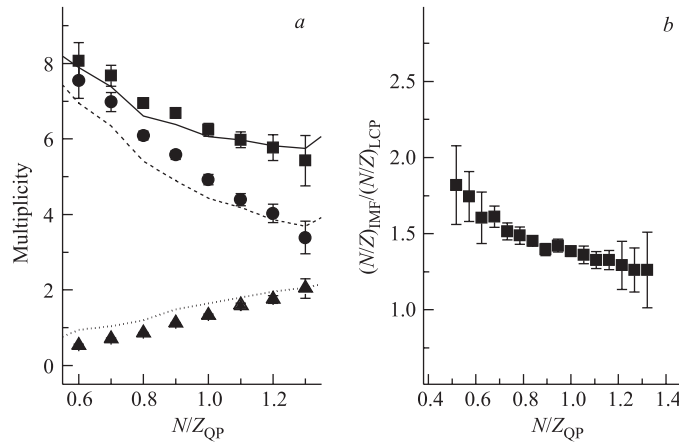


Fig. 24. *a*) Multiplicity of charged fragments (■), LCPs (●) and IMFs (▲) versus N/Z_{QP} . Corresponding lines represent the DIT/SMM calculation. *b*) Experimental ratio of the mean values of N/Z of LCPs and IMFs versus the N/Z_{QP} . Data are given for the reaction $^{28}\text{Si} (50 A \cdot \text{MeV}) + ^{112}\text{Sn}$ [49]

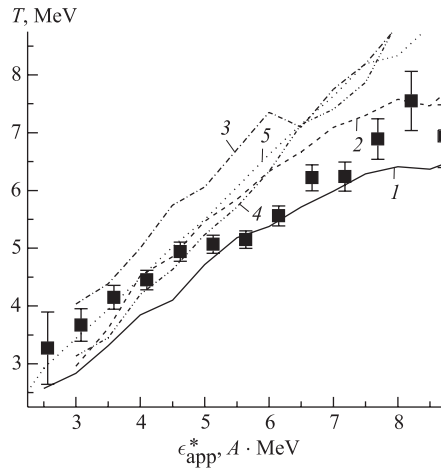


Fig. 25. Comparison of temperature obtained using the double isotope ratio thermometer $d, t/{}^3\text{He}, {}^4\text{He}$ [44] (■) with kinematic temperatures of p (1), d (2), t (3), ${}^3\text{He}$ (4), ${}^4\text{He}$ (5) in the c.m. frame of quasi-projectiles

quasi-projectile frame (see Fig. 25). While at low excitation energies the double isotope ratio thermometer $d, t/{}^3\text{He}, {}^4\text{He}$ represents essentially an average of the kinematic temperatures of individual species, in the plateau region there occurs a transition to the regime where the double isotope ratio temperature represents the kinematic temperature of protons (and possibly of the nucleon gas). Such a transition, just above the turning-point where the isovector part of chemical potential deviates from the trend of homogeneous system (as shown in Fig. 23), suggests that the isotopic composition of fragments is in equilibrium with the free nucleon gas what is a basic assumption used in grand-canonical models such as SMM [5]. The higher values of kinematic temperatures of $d, t, {}^3\text{He}, {}^4\text{He}$

suggest that the clusters are created prior to such equilibration (possibly by spinodal decomposition). On the other hand, the low energy behavior can be explained

by an assumption that the isotopic composition is determined at the instant when clusters are emitted what is in good agreement with our understanding of the compound nucleus de-excitation [12]. The two different values of heat capacities in low- and high-energy parts of the caloric curve, suggested in Fig. 23, *b*, can thus be understood as representing a homogeneous nuclear liquid and an isospin-asymmetric free nucleon gas, respectively.

Apart from signatures of the first-order phase transition, several experimental works [17, 64], exploring observed mass (charge) distributions, report a critical behavior in the multifragmentation data, which can be understood as a signal of the second-order phase transition at the critical temperatures between 5–10 MeV [65]. However, multifragmentation studies employing the statistical model analysis of charge distribution [66] suggest the value of critical temperature above 15 MeV. Besides of raising obvious questions concerning the applicability of used methods of analysis, such contradictory observations may in principle suggest a complex phase diagram, possibly analogous to the Ising model, where both first-order and second-order can be observed. It is also possible that the observed critical behavior is a specific feature of the finite system, as suggested in theory [67]. The recent experimental work where the critical behavior is related to the size of the largest fragment as an order parameter [68] supports such assumptions. The finite-size effect can play role also in the multifragmentation of quasi-projectiles with $A = 20\text{--}30$ and thus similar analysis for heavier sources is necessary to evaluate the role of such effect and establish the link to the phase transition in the isospin-asymmetric nuclear matter at subsaturation densities. It may be however noted that theoretical studies of small systems [9] suggest that Van der Waals-like loops observed in infinite systems are affected in transition to finite system only by small terms and thus the conclusions for finite systems can be in principle applicable also for infinite case.

SUMMARY AND CONCLUSIONS

In this article we have presented an overview of the recent progress in the studies of nuclear multifragmentation. Theoretical and experimental concepts relevant to investigation of isotopic trends in nuclear multifragmentation were described and the possibilities to extract the physical information on the nuclear equation of state were outlined. A special emphasis was put on the methods how the isotopic composition of fragments can be used to extract the values of thermodynamical observables of the system undergoing multifragmentation such as temperature and chemical potentials (free nucleon densities). Various methods for extraction of thermodynamical variables were presented and possibilities of their using were documented on examples of multifragmentation data. It was shown that the yield ratios of specific isotopes from statistical multifragmentation

typically exhibit an exponential scaling with various observables. The logarithmic slopes of such dependences can be related to thermodynamical observables such as grand-canonical temperatures (isotopic thermometers) or chemical potentials (isoscaling). Finally, an extensive overview of investigations of multifragmentation of the fully reconstructed quasi-projectiles is presented. The dominant reaction mechanism is determined as binary nucleus–nucleus collisions with intense dissipation and heating via nucleon exchange. The implications of the fragment data concerning the isospin-asymmetric liquid–gas phase transition in the nuclear matter are discussed. Multiple correlated signals point toward observation of a first-order phase-transition in the quasi-projectile multifragmentation data.

Acknowledgements. The author acknowledges fruitful collaboration with research groups of Professors S. J. Yennello and J. B. Natowitz during his stay at Cyclotron Institute of Texas A&M University. Examples from the analysis of experimental data acquired using FAUST and NIMROD arrays are used throughout this work to illustrate the use of reviewed methods. Insightful comments from A. I. Sanzhur and P. I. Zarubin are gratefully acknowledged. This work was supported by the Slovak Scientific Grant Agency through grant VEGA-2/5098/25.

REFERENCES

1. *Moretto L. G., Wozniak G. J.* // *Ann. Rev. Nucl. Part. Sci.* 1993. V. 43. P. 379.
2. *Proc. of Intern. Conf. CRIS-2000, Catania, 2000; Nucl. Phys. A.* 2001. V. 681; *Proc. of Intern. Conf. NN-2003, Moscow, 2003; Nucl. Phys. A.* 2004. V. 734.
3. *Silberberg R., Tsao C. H.* // *Phys. Rep.* 1990. V. 191. P. 351.
4. *Richert J., Wagner P.* // *Phys. Rep.* 2001. V. 350. P. 1.
5. *Bondorf J. P. et al.* // *Phys. Rep.* 1995. V. 257. P. 133.
6. *Müller H., Serot B. D.* // *Phys. Rev. C.* 1995. V. 52. P. 2072.
7. *Li B.-A., Ko C.* // *Nucl. Phys. A.* 1997. V. 618. P. 498; *Baran V. et al.* // *Phys. Rev. Lett.* 2001. V. 86. P. 4492; *Colonna M. et al.* // *Phys. Rev. Lett.* 2002. V. 88. P. 122701; *Marqueron J., Chomaz P.* // *Phys. Rev. C.* 2003. V. 67. P. 41602(R).
8. *Gross D. H. E.* // *Phys. Rep.* 1997. V. 279. P. 119.
9. *Hill T. L.* *Thermodynamics of Small Systems.* N. Y.; Amsterdam: W. A. Benjamin Publishers, 1963.
10. *Veselsky M. et al.* // *Phys. Rev. C.* 2000. V. 62. P. 064613.
11. *Veselsky M. et al.* // *Nucl. Phys. A.* 2003. V. 724. P. 431.
12. *Hauser W., Feshbach H.* // *Phys. Rev.* 1952. V. 87. P. 366.
13. *Moretto L. G.* // *Nucl. Phys. A.* 1975. V. 247. P. 211.
14. *McMahan M. A. et al.* // *Phys. Rev. Lett.* 1985. V. 54 P. 1995.
15. *Charity R. et al.* // *Nucl. Phys. A.* 1988. V. 483. P. 391.

16. Lopez J. A., Randrup J. // Nucl. Phys. A. 1989. V. 503. P. 183.
17. Kreuzt P. et al. // Nucl. Phys. A. 1993. V. 556. P. 672.
18. Sauer G., Chandra H., Mosel U. // Nucl. Phys. A. 1976. V. 264. P. 221.
19. Siemens P. J. // Nature. 1983. V. 305. P. 410.
20. Kolomietz V. M. et al. // Phys. Rev. C. 2001. V. 64. P. 24315.
21. Fisher M. E. // Physics. 1967. V. 3. P. 255.
22. Bugaev K. A. et al. // Phys. Rev. C. 2000. V. 62. P. 044320; Phys. Lett. B. 2001. V. 498. P. 144; Reuter P. T., Bugaev K. A. // Ibid. V. 517. P. 233.
23. Hammersley J. M. // Proc. of the 87th Intern. Colloq. CNRS. Paris, 1957. P. 17.
24. Veselsky M. // Nucl. Phys. A. 2002. V. 705. P. 193.
25. Souliotis G. A. et al. // Phys. Lett. B. 2002. V. 543. P. 163; Phys. Rev. Lett. 2003. V. 91. P. 022701.
26. Guthrie M. P., Alsmiller R. G., Bertini H. W. // Nucl. Instr. Meth. 1968. V. 66. P. 29; Barashenkov V. S., Toneev V. D. High-Energy Interactions of Particles and Nuclei with Nuclei. 1972 (in Russian).
27. Schuttauf A. et al. // Nucl. Phys. A. 1996. V. 607. P. 457.
28. Negele J. W. // Rev. Mod. Phys. 1992. V. 54. P. 913.
29. Kruse H., Jacak B. V., Stoecker H. // Phys. Rev. Lett. 1985. V. 54. P. 289; Molitoris J., Stoecker H. // Phys. Rev. C. 1985. V. 32. P. 346; Molitoris J., Stoecker H., Winer B. // Phys. Rev. C. 1987. V. 36. P. 220.
30. Bertsch G., Gupta S. // Phys. Rep. 1988. V. 160. P. 189; Cassing W. et al. // Phys. Rep. 1990. V. 188. P. 363.
31. Gregoire C. et al. // Nucl. Phys. A. 1987. V. 465. P. 317; V. 471. P. 399c; Schuck P. et al. // Prog. Part. Nucl. Phys. 1990. V. 22. P. 181.
32. Bonasera A. et al. // Phys. Rep. 1994. V. 243. P. 1.
33. Aichelin J. // Phys. Rep. 1991. V. 202. P. 233.
34. Gimeno-Nogues F. et al. // Nucl. Instr. Meth. A. 1997. V. 399. P. 94.
35. Marie N. et al. // Progress in Research, 1997–1998. Cyclotron Institute, Texas A&M University. College Station, 1998. P. V-19; Wada R. et al. // Progress in Research, 1998–1999. Cyclotron Institute, Texas A&M University. College Station, 1999. P. V-15.
36. Veselsky M. et al. // Progress in Research, 2000–2001. Cyclotron Institute, Texas A&M University. College Station, 2001. P. V-13.
37. Tassan-Got L. // Nucl. Instr. Meth. B. 2002. V. 194. P. 503.
38. Veselsky M., Souliotis G. A., Yennello S. J. // Proc. of the 5th Intern. Conf. DANF-2001, Casta-Papiernicka, Slovakia, 2001. World Scientific, 2002. P. 461.
39. Shetty D. V. et al. // Phys. Rev. C. 2003. V. 68. P. 54605.
40. Frankland J. D. et al. // Nucl. Phys. A. 2001. V. 689. P. 905.
41. Cavata C. et al. // Phys. Rev. C. 1990. V. 42. P. 1760.
42. Wada R. et al. // Phys. Rev. Lett. 1987. V. 58. P. 1829; Barz H. W. et al. // Phys. Lett. B. 1988. V. 211. P. 10; Yennello S. J. et al. // Phys. Lett. B. 1994. V. 321. P. 14; Johnston H. et al. // Phys. Lett. B. 1996. V. 371. P. 186; Ramakrishnan E. et al. // Phys. Rev. C. 1998. V. 57. P. 1803.

43. *Fuchs H., Möhring K.* // Rep. Prog. Phys. 1994. V. 57. P. 231.
44. *Veselsky M. et al.* // Phys. Lett. B. 2001. V. 497. P. 1.
45. *Albergo S. et al.* // Nuovo Cim. 1995. V. 89. P. 1.
46. *Randrup J., Koonin S. E.* // Nucl. Phys. A. 1981. V. 356. P. 223.
47. *Hauger J. A. et al.* // Phys. Rev. Lett. 1995. V. 77. P. 235;
Xi H. et al. // Z. Phys. A. 1997. V. 359. P. 397;
Ruangma A. et al. // Phys. Rev. C. 2002. V. 66. P. 44603.
48. *Tsang M. B. et al.* // Phys. Rev. Lett. 1997. V. 78. P. 3836.
49. *Veselsky M. et al.* // Phys. Rev. C. 2000. V. 62. P. 41605(R).
50. *Xu H. S. et al.* // Phys. Rev. Lett. 2000. V. 85. P. 716.
51. *Tsang M. B. et al.* // Phys. Rev. Lett. 2001. V. 86. P. 5023.
52. *Botvina A. S. et al.* // Phys. Rev. C. 2002. V. 65. P. 44610.
53. *Lozhkin O. V., Trautmann W.* // Phys. Rev. C. 1992. V. 46. P. 1996.
54. *Souliotis G. A. et al.* // Phys. Rev. C. 2003. V. 68. P. 24605.
55. *Veselsky M., Souliotis G. A., Jandel M.* // Phys. Rev. C. 2004. V. 69. P. 44607.
56. *Souliotis G. A. et al.* // Phys. Lett. B. 2004. V. 588. P. 35.
57. *Veselsky M., Souliotis G. A., Yennello S. J.* // Phys. Rev. C. 2004. V. 69. P. 31603(R).
58. *Laforest R. et al.* // Phys. Rev. C. 1999. V. 59. P. 2567.
59. *Tassan-Got L., Stéfan C.* // Nucl. Phys. A. 1991. V. 524. P. 121.
60. *Pochodzalla J. et al.* // Phys. Rev. Lett. 1995. V. 75. P. 1040.
61. *Natowitz J. B. et al.* // Phys. Rev. C. 2002. V. 65. P. 34618.
62. *D'Agostino M. et al.* // Nucl. Phys. A. 1999. V. 650. P. 329.
63. *Borderie B. et al.* // Phys. Rev. Lett. 2001. V. 86. P. 3252.
64. *Minich R. W. et al.* // Phys. Lett. B. 1982. V. 118. P. 458;
Panagiotou A. D. et al. // Phys. Rev. Lett. 1984. V. 52. P. 496;
Elliot J. B. et al. // Phys. Rev. C. 2000. V. 62. P. 64603.
65. *Elliot J. B. et al.* // Phys. Rev. Lett. 2002. V. 88. P. 42701;
Berkenbusch M. K. et al. // Ibid. P. 22701.
66. *Karnaukhov V. A. et al.* // Phys. Rev. C. 2003. V. 67. P. 011601(R).
67. *Biro T. S., Knoll J., Richert J.* // Nucl. Phys. A. 1986. V. 459. P. 692;
Botet R., Ploszajczak M. // Phys. Rev. E. 2000. V. 62. P. 1825.
68. *Frankland J. D. et al.* nucl-ex/0404024. 2004.